Modal analyses of rotor wakes by means of time-resolved PIV measurements

G. Ceglia[1, *], F. De Gregorio[1]

1: Lab. of Aerodynamic Measurement Methodologies, CIRA Italian Aerospace Research Centre, Italy

* g.ceglia@cira.it

Keywords: rotary-wing aerodynamics, tip vortex interaction, modal analyses, time-resolved PIV

ABSTRACT

Data-driven decomposition methods, i.e., Proper Orthogonal Decomposition (POD) and Dynamic Mode Decomposition (DMD), have been exploited for analyzing time-resolved PIV measurements of tip vortices shed by a four-bladed isolated rotor in hovering conditions. Two rotor speeds at either $\omega = 2\pi \cdot 29.9$ H z or $2\pi \cdot 26.3$ Hz have been explored, defining two test cases TC1 or TC2, respectively. Under these regimes, the corresponding aerodynamic loads, in terms of thrust coefficient, lead to $C_T = 5.5 \times 10^{-3}$ or 5.4×10^{-3}, and, of figures of merit, $FM = 0.47$ or 0.46, respectively. The travel of the tip vortices determines on average a wake contraction inward the radial direction, which effect is more pronounced as the thrust diminishes. During their evolution, momentum addition of the quiescent ambient air is imposed by the advection of the corotating vortex travel. This culminates further downstream where the pairing process of two consecutive vortices occurs. These dynamical mechanisms have been studied in detail using modal analyses. The dominance of the periodic shedding of the tip vortices was captured by both the modal decompositions. The first pair of POD modes describe the spatial organization of the tip vortices and the pairing region. The corresponding time coefficients include multiple frequency peaks discerning the most prominent contribution ascribed to the tip vortex shedding. Dually, the analysis by the DMD method indicates the tip vortices as the most dynamic flow feature. Secondary flow structures are found for TC1 in correspondence of the shear layer and the developed wake, having a characteristic frequency of the order of the rotor speed. Whereas for TC2 it is found that small vortical structures concur to the build-up of the complete vortical dynamic, they are characterized by a doubled frequency than that measured for the tip vortices.

1   Introduction

The aerodynamic of the wake of a helicopter main rotor exhibits intricate characteristics typical of high three-dimensional and unsteady flows containing tip vortices and vortex sheets (De Gregorio et al. (2012)). Large eddies and energetic turbulence create a highly complex flow environment difficult to inspect. The interaction between the blade structure and such unsteady aerodynamic loads determines persistent stress, whose prediction is crucial for the design and development of the rotor blades themselves (Brocklehurst & Barakos, 2013).

In hover, the tip vortices travel down along the vertical direction, following a nominal three-dimensional (3D) elliptical path below the rotor (Leishman & Bagai, 1998). Leishman and Bagai

(1998) investigated these vortical patterns through flow visualizations and phase resolved measurements for wakes generated by a two-blades propeller. They pointed out that, even in hover conditions, the periodicity of the wakes embeds an aperiodic spatial organization of the vortices. This can be ascribed by turbulent mechanisms promoted by vortex interactions. Bhagwat and Leishman (2000) investigated the velocity profiles of tip vortices shed by one- and two-bladed rotors in hovering by means of three-component laser Doppler velocimetry. They found a pronounced self-similarity shape of the swirl velocity component at different locations. However, as the vortex age increases a vigorous viscous diffusion was observed. In this direction, Jain and Conlisk (2000) studied the interaction of tip vortices shed by a two-bladed rotor, they described the pairing process occurring between two consecutive co-rotating vortices. They also pointed out that this interaction behaves in a periodic and deterministic manner. The diffusive viscous effects are emphasized when the wake approaches a solid boundary as described by Ramasamy and Leishman (2004). In their work, constraints to the wake affect the flow pattern promoting velocity gradients and vortex stretching. Successively, the same research team studied the formation and evolution of the tip vortices generated by a hovering rotor by means of dual-plane stereoscopic Particle Image Velocimetry (PIV) measurements Ramasamy et al. (2009). They exploited the advantages of the dual PIV technique to retrieve the velocity gradient tensor, so that, unveiling the turbulent flow features participating to the tip vortex evolution. They pointed out that the core of the tip vortices behaves without the assumption of isotropic turbulence.

The PIV technique has proven as a reliable tool for the investigation of such complex flows. A survey has been presented by Raffel et al. (2012), in which experiments in challenging configurations have been extensively outlined with regard to understating helicopter aerodynamics. Two- and three-components PIV measurements were conducted by Richard et al. (2006) to track tip vortices from their onset to half cycle of a four-bladed rotor in hover conditions. They pointed out the needing of enlarging the overlap degree between the interrogation windows to reduce random sampling artefacts arising during the correlation process. Mula and Tinney (2015) investigated the turbulent features of a tip vortex generated by a single-bladed rotor in hover using Proper Orthogonal Decomposition (POD, Sirovich (1987)). The rolling-up of the vortical structure was found to be dominated by a helical mode, which is the most energetic.

The present study deals with an experimental investigation on the flow characteristics of rotor wakes by means of Time-Resolved (TR) PIV measurements. A four-bladed rotor generates the wake flows in hover conditions. The focus is placed upon the study of coherent vortical structures periodically shed from the blade tip, their dynamic and spatial organization. The main questions driving the need for TR-PIV measurements are how the travelling vortical structures interact

triggering their coalescence and the role of the frequencies participating in the periodic phenomenon. To unveil the basic and dynamical mechanisms of these flow structures, data-driven analyses, e.g., POD and Dynamic Mode Decomposition (DMD, Schmid (2010)), have been used.

2 Experimental setup and test cases

The tests were carried out at the Aerodynamic Measurement Methodology laboratory in CIRA. The experiments were conducted with the aim of studying the flow organization and dynamic evolution of rotor wakes. These were generated by a four-blade rotor of an existing commercial radio-controlled helicopter model (Blade 450 3D RTF) operated in hover conditions. It is worth underline that the tail boom and tail rotor were not considered for this study. The rotor rig was developed in the framework of the Garteur AG22 and already investigated by standard 2C-PIV measurements in De Gregorio et al. (2021). The arrangement of the experimental setup is shown in the picture in Fig. 1. The blades have a rectangular planform of span length of $R = 0.36$ m, thus covering a diameter of $D = 0.72$ m, and chord length of $c = 0.0327$ m. The airfoil section follows a NACA 0013 shape along the span direction. The root cut-out is at 16% of the radius, thus resulting a rotor solidity of 0.116. The maximum rotational speed attains to $\Omega = 1800$ rpm in clockwise direction, able to vary the collective pitch angle between 0° up to 12.2°.

For the experiments, the rotor rig was placed at the mid-distance from the walls of a rectangular room of 5.2 m long and 4.5 m wide, thus, ensuring a minimum distance from the rotor tip to the walls of 1.40 m (1.94 D). The rotor was installed at a height of 2.5 D, avoiding the presence of ground effects in agreement with the findings carried out by Prouty (1985). Complementarily, the distance from the roof was at 1.53 D, larger than the threshold value of 0.5 D indicated by Rossow (1985). Therefore, wall and ground effects due to the confinement are considered negligible for the present experimental setup. The aerodynamic loads were measured by means of a six-component balance of type of Mini 40 manufactured by ATI installed at the interface between the model and the holder. The balance was set with calibration at full scale (FS) of ±60 N along the vertical direction, with an accuracy of 0.60 N; whereas, the FS of the momentum (torque) was ±1 Nm with an accuracy of 0.0150 Nm.

The inspection of the evolution of the rotor wakes was performed by time resolved (TR) two-component PIV measurements. Aerosolized diethylhexylsebacate (DEHS) droplets of diameter less than 1 μm were used as tracer particles produced by a seeding generator equipped with 20 Laskin nozzles. A homogenous concentration of the particles was reached in the room. The illumination was provided by a Photonics DM 30 dual head Nd-YLF laser with a pulse energy of 20 mJ at the wave length of 527 nm for an operating frequency of $f_s = 2.16$ kHz. The time separation between the laser pulses was set at 40 μs. Three high speed cameras were installed vertically and

in parallel, slightly staggered for following the contraction of the rotor wake, as illustrated in the picture of **Fig. 1**. Two Phantom VEO 710L cameras (7400 frame rate, 1280×800 pixels, 12-bit, pixel dimension 20 μm) and a Phantom VEO 640L model (1400 frame rate, 2560×1600 pixels, 12-bit, pixel dimension 10 μm) were used. For this latter, a reduced resolution of 1280 × 800 pixel was set to operate it at the considered acquisition rate (f_s). Each VEO 710 camera was equipped with a Nikkor lens of focal length of 200 mm with aperture set at $f\# = 5.6$. Whereas, the VEO 640 camera mounted a Zeiss lens with a focal length of 100 mm set at an aperture of $f\# = 2.8$. The final measurement region covers an area of size of 96.3 × 190.8 mm², partially overlapped between each camera imaging. This yields a spatial resolution of 15.93 pixel/mm. The periodic phenomenon was sampled by synchronizing the TR-PIV system through a hall effect trigger monitoring the rotational speed as well of the rotor rig. Two rotational speeds were considered either $\omega = 2\pi \cdot 29.9$ Hz or $2\pi \cdot 26.3$ Hz. In correspondence, an amount of 30 cycles was captured by discretizing each one in 72 or 82 phases. The calibration was performed using a double plane target covering all the measurement domain. The mapping functions are generated using the pinhole as a fit model with a maximum fit error equal to about 0.28 pixel. This procedure reduces the effects introduced by the different viewing angle of each camera (see **Fig. 1**) and, also, allows for the stitching of the particle images acquired by the three cameras. The raw images were pre-processed through local filters by equalizing the particle intensity considering a local normalization filter of 300 pixels size. This reduces the presence of intensity gradients all over the image. The particle field motion was computed by an iterative multi–grid cross–correlation algorithm ending at 32 × 32 pixels with 75% of overlap using LaVision software Davis 10.1. The final vector pitch attains to 0.50 mm. This ensures to spatially resolve the vortices by placing at least 10 vectors along the radial direction of each detected vortex. A median filter with universal outlier detection (Westerweel & Scarano, 2005) was applied as a vector validation method for a filter region of 5 × 5 vectors. However, any clusters of spurious vectors, if present, are rejected by a 4-pass spatial median filter, removing groups of less than eight false vectors. The empty spaces left by the validation process are filled up by interpolated vectors with the average calculated over all the non-zero neighbor vectors.

The computation of the displacement vector intrinsically provides an evaluation of the level of uncertainty by considering the differences between two overlapped interrogation windows mapped onto each other (Wieneke, 2017). The particle diameter measures about 1.5 pixels, the uncertainty of the velocity vector results in average of 0.83 m/s evaluated in the shear layer region by means of the Davis 10.2 software (Wieneke, 2015).
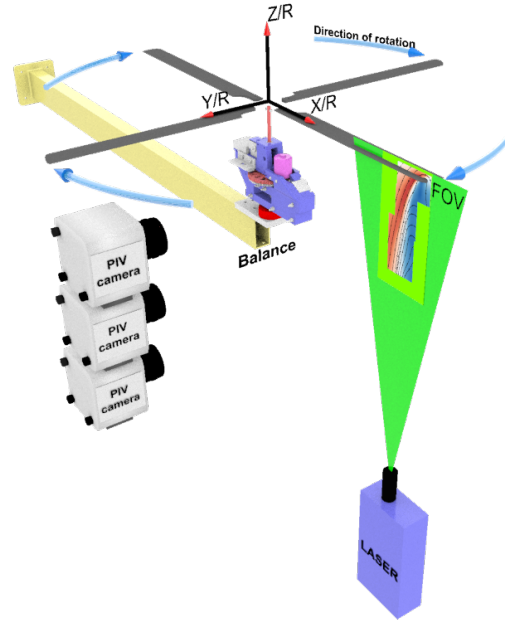
Fig. 1 Schematic of the experimental setup: rotor rig and TR-PIV system; measurement region with the field of view and the reference frame.

The current study addresses test cases in which the angular velocity of the rotor was set either at ω = 2π·29.9 Hz or 2π·26.3 Hz, identifying two test conditions named herein TC1 or TC2, respectively. The collective angle of the blade plate was set at 11.2° for both cases. Consequently, the component of the vertical force (thrust) and the corresponding torque attain T = 12.5 N and Q = 0.505 Nm for the TC1, respectively; whereas they result in T = 9.75 N and Q = 0.397 Nm for the TC2. The trust coefficient C_T and the figure of merit FM, respectively, are defined in Eqs. (1) and (2).

$$C_T = \frac{T}{\rho \pi R^2 (\omega R)^2} \tag{1}$$

$$FM = \frac{TR\sqrt{C_T/2}}{Q} \tag{2}$$

Where the ρ is the air density (1.18 kg/m³). The hover induced velocity V_h, evaluated from the momentum theory, reads as in Eq. (3).

$$V_h = \omega R\sqrt{C_T/2} \tag{3}$$

The test parameters and the values of the main aerodynamic parameters are summarized in Table 1.

Table 1 Parameters of the measured test cases.

Parameters	TC1	TC2
Rotor frequency, $\omega/2\pi$ [Hz]	29.9	26.3
Trust cefficient, C_T	5.5 × 10⁻³	5.4 × 10⁻³
Figure of merit, FM	0.47	0.46

Hover induced velocity, V_h [m/s]	3.608	3.185

3 Results and discussion

In the following, the velocity components along the directions X and Z are indicated by the symbols U and W, respectively. The corresponding lower-case letters, u and w, refer to the components of the turbulent velocity fluctuations. The results are presented in dimensionless form considering the blade chord c, the hover induced velocity, V_h, and the rotor radius, R, as reference quantities.

3.1 Average flow fields

The flow characteristics of the rotor wakes are inspected through the time-average flow fields, the overbar indicates the operation of ensemble averaging. Fig. 2 shows the iso-contours of the absolute time-average velocity field $|\bar{V}|/V_h$ for TC1 (a) and TC2 (b) at the meridional plane illustrated in Fig. 1. For both cases, the magnitude of the absolute velocity increases inward of the blade tip along the vertical direction reaching its maximum of $|\bar{V}|/V_h = 2.7$. The isolines of $|\bar{V}|/V_h = 0.6$ and $|\bar{V}|/V_h = 2$ enclose the shear layer region highlighting the wake contraction towards the rotor axis. This is more pronounced as close as the wake is to the rotor disk. As expected, the strength of the wake persists even down to negative vertical locations for the case TC1, reflecting the higher value of $C_T = 5.4 \times 10^{-3}$ (Table 1). However, more contraction of the wake towards the rotor axis is observed in the periphery of the investigated region, i.e., -0.5 ≤ Z/R ≤ -0.4, for the case at slightly lower $C_T = 5.4 \times 10^{-3}$ (TC2).
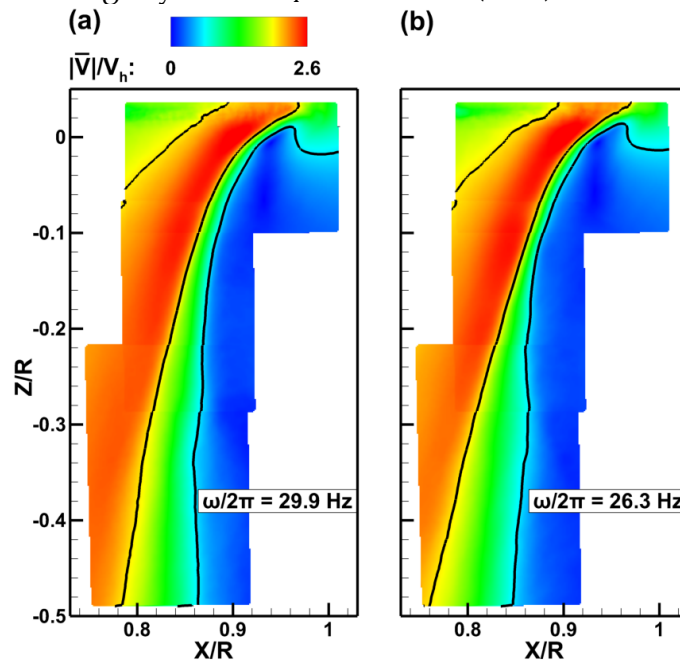

Fig. 2 Iso-contours of the time-average absolute velocity field $|\bar{V}|/V_h$ with isolines of $|\bar{V}|/V_h = 0.6$ and $|\bar{V}|/V_h = 2$ for the test cases TC1, at $\omega/2\pi = 29.9$ Hz (a), and TC2, at 26.3 Hz (b).

The root mean square (rms) of the radial velocity fluctuation is depicted in Fig. 3 for TC1 (a) and TC2 (b) at the meridional plane. Concentrations of the radial velocity fluctuation are located in the proximity of the rotor disk, where the onset of the vortical structures occurs at the blade passages. The peak activity intensifies as the contraction of the wake has the maximum inclination with respect to the horizontal direction, which measures ~30.3° and ~32.0° for TC1 and TC2, respectively. Down to $Z/R \leq$ -0.015, the wake contraction flattens again approaching the vertical direction, the peak activity undergoes a decreasing of intensity more pronounced for the TC1 case. A detailed inspection of the map in Fig. 3 (a) reveals the presence of two preferred vortical paths between -0.26 $\leq Z/R \leq$ -0.12 as testified by the peaks of u_{rms}/V_h.
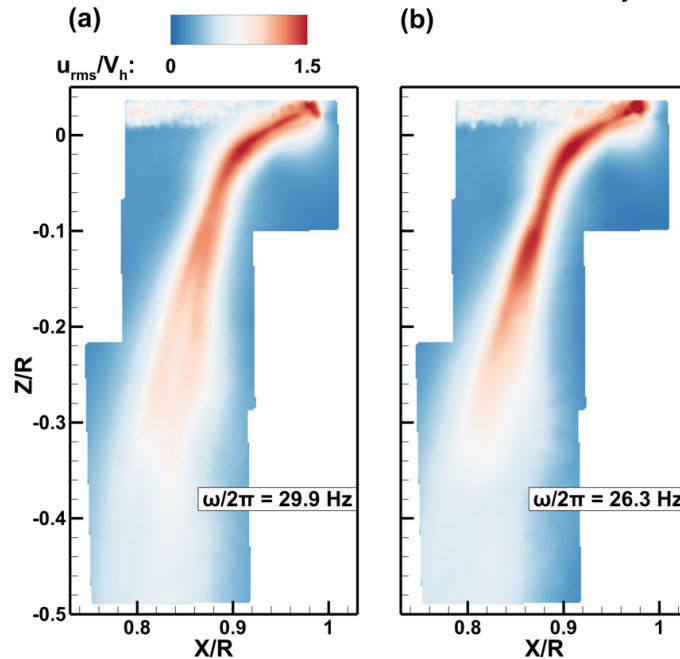

Fig. 3 Iso-contours of the rms radial velocity fluctuation u_{rms}/V_h for the test cases TC1, at $\omega/2\pi =$ 29.9 Hz (a), and TC2, at 26.3 Hz (b).

3.2 Instantaneous flow fields

The evolution of the vortical structures is investigated by the instantaneous flow fields. The basic flow organization is unveiled by the identification of the tip vortices evolving in the inward side of the rotor wakes. Since the shedding of the tip vortices has intrinsically periodic features, the time coordinate refers to the position of the blade at each azimuth angle Ψ (see **Fig. 1**). Hence, the phenomenon was sampled every $\Delta\Psi = 5°$ for TC1. Since part of the blade was imaged in the FOV, for convenience, the reference at $\Psi = 0°$ was set in correspondence with one blade passage. As an example, **Fig. 4** shows the iso-contours of the instantaneous out-of-plane vorticity $\omega_Y c/V_h$ with in-plane velocity vectors at different azimuth angles, $\Psi = 0°$, 45° and 90°. This describes the formation of the tip vortex and the pairing process due to their interaction. Four co-rotating vortices are recognized at $\Psi = 0°$, they were shed during the revolution of the blade tips having vortex ages Ψ_V

= 90°, 180°, 270° and 360°, as expected for a four bladed rotor. Here, the vortex age Ψ_V is defined as the azimuthal position (from the reference $\Psi = 0°$) of the blade that shed the respective travelling vortex (Braukmann et al. (2019)). These vortices feature different spacing between each other of experiencing convective velocity values of $|V|/V_h = 2.88$, 1.60, 0.65 and 0.51 for the vortices at ages $\Psi_V = 90°$, 180°, 270° and 360°, respectively. The two co-rotating vortices in the middle ages, 180° and 270° lie at a distance sufficiently closer to trigger the pairing process. Hence at $\Psi = 45°$, this interaction promotes the engulfment of their spatial organization, the pursuer vortex influences the trajectory of the preceding one as shown in the map of **Fig. 4**(b). Furthermore, the complete passage of the blade determines the formation of an additional tip vortex as testified by the vorticity concentration $\omega_Y c/V_h = 173$ at $Z/R = 0.011$. The aged vortices travel along the vertical direction following the path enclosed in the shear layer region. During their travel, the entrainment of ambient quiescent air strengthens the rotor wake through momentum addition. However, viscous effects impose a reduction of the convective velocity of each aged vortex, promoting turbulent dissipation mechanisms. At $\Psi = 90°$, the pairing process culminates in the merging of the two vortical structures with peak activity of $\omega_Y c/V_h = 60$ at the vertical location $Z/R = -0.3$ (**Fig. 4**c). Similar observations can be found in the vortical evolution of the test case TC2, for the sake of conciseness not presented herein.
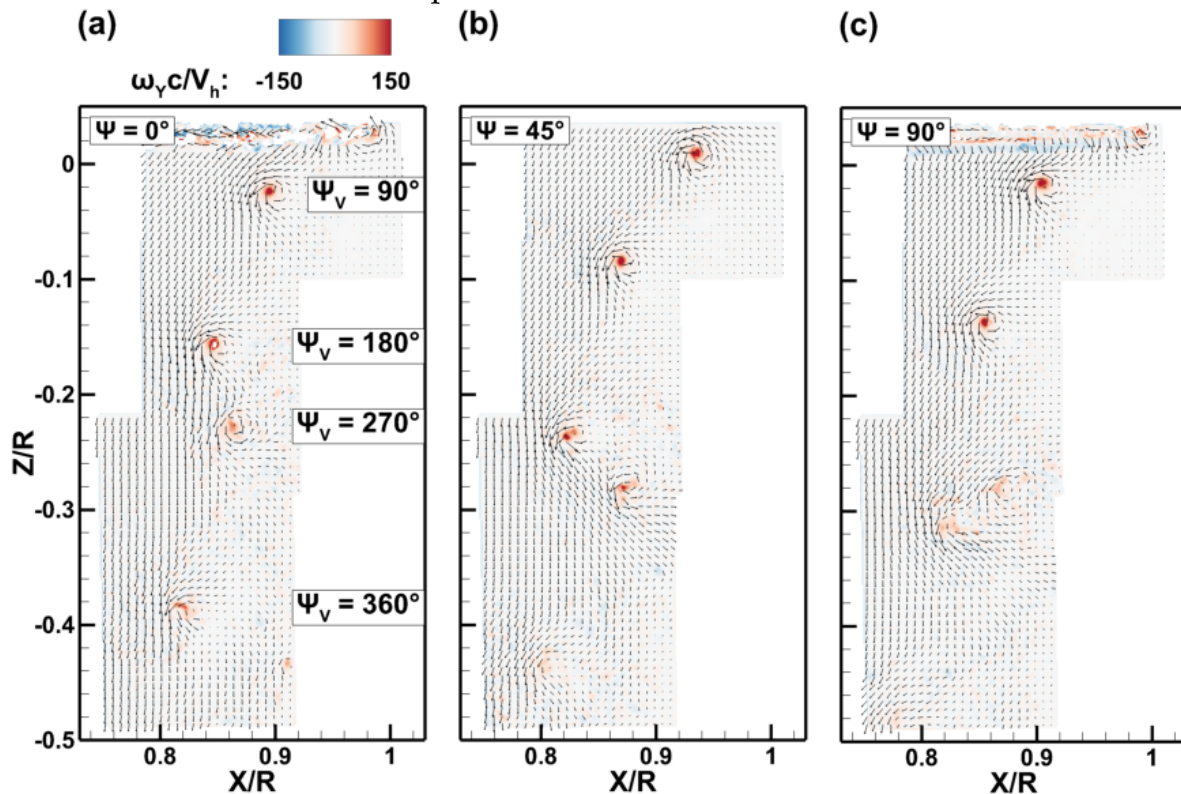

Fig. 4 Instantaneous velocity fields of TC1 ($\omega/2\pi = 29.9$ Hz): iso-contours of out-of-plane vorticity $\omega_Y c/V_h$ with in-plane velocity vectors placed every five measured points at azimuth positions $\Psi = 0°$ (a), 45° (b) and 90° (c); vortex ages reported in (a).

3.3   Modal analyses

To fix the notation, data-driven decomposition methods, such as, snapshot-POD (Sirovich, 1987), dynamic mode decomposition (DMD) (Schmid, 2010), are briefly introduced. Considering a data set of N realizations uniformly discretized in time and represented by the velocity vector $\underline{V}(\underline{X}, t)$, it is decomposed into the sum of its time-average $\overline{\underline{V}(\underline{X}, t)}$ and fluctuating part $\underline{v}(\underline{X}, t)$. The decompositions are based on the entire data set for either test cases TC1 or TC2, which amount to 2130 or 2370 TR-PIV snapshots, respectively. To isolate the energy contribution pertaining to only the flow structures, the portion of the measured region containing the passage of the blade is excluded from the region of interest.

The POD is applied to decompose the flow field, exploiting an energy optimality approach, that ensures the identification of the most energetic flow structures arranged hierarchically within a few modes. The velocity fluctuation $\underline{v}(\underline{X}, t)$ is approximated by a set of orthonormal basis functions $\underline{\varphi}_n(\underline{X})$ optimized in the last square sense and by linearly combining them with a proper set of temporal structures $\mu_n(t)$ weighted by σ_n as reading in Eq. (4).

$$\underline{v}(\underline{X}, t) \approx \sum_{n=1}^{N} \sigma_n \mu_n(t) \underline{\varphi}_n(\underline{X}) \tag{4}$$

In the snapshot-POD method (Sirovich, 1987), the eigenmode decomposition of the two-point temporal correlation matrix, defined as $R_{ij} = \overline{\underline{v}(X_i, t) \cdot \underline{v}(X_j, t)}$, leads to the evaluation of the eigenvalues λ_n representative of the level of kinetic energy associated with the eigenmodes, i.e., the temporal structures $\mu_n(t)$, already introduced in the decomposition of the velocity field. The POD modes $\underline{\varphi}_n(\underline{X})$ are retrieved by projecting the velocity fluctuation $\underline{v}(\underline{X}, t)$ into the temporal structure $\mu_n(t)$ scaled by the amplitude $\sigma_n = \sqrt{\lambda_n}$, as formulated in Eq. (5).

$$\underline{\varphi}_n(\underline{X}) = \frac{1}{\sigma_n} \sum_{i=1}^{N} \underline{v}(\underline{X}, t_i) \mu_n(t_i) \tag{5}$$

Where the sum is calculated over the time coordinate t.

Considering the time-dependent behavior of the investigated phenomenon, the DMD is used to unveil the pertinence of the spatial structures, e.g., found by means of POD, with Fourier analysis in time. The coherent structures evolve in time through characteristic frequencies, their amplitudes can undergo dampening or growing. Thus, the DMD is particularly suitable in conduct stability analysis of time-dependent flow fields. The decomposition of $\underline{V}(\underline{X}, t)$ is based on the low-rank approximation, reduced by the r order, of the eigenvalues $\omega_n^{(r)}$ and eigenvectors $\underline{\varphi}_n^{(r)}(\underline{X})$ of the linear operator A in the dynamical system of Eq. (6).

$$\underline{V}(\underline{X}, t_{i+1}) = A \, \underline{V}(\underline{X}, t_i) \tag{6}$$

Thus, the approximate solution of Eq. (6), calculated as the minimization in least square sense (Schmid, 2010), reads as Eq. (7).

$$\underline{V}(\underline{X}, t) \approx \sum_{n=1}^{r} a_n^{(r)} \underline{\varphi}_n^{(r)}(\underline{X}) e^{\omega_n^{(r)} t} \tag{7}$$

Where $a_n^{(r)}$ the initial amplitude of the DMD modes. In particular, being the eigenvalues $\omega_n^{(r)}$ complex, their real and imaginary parts contribute to the evaluation of the amplification coefficient, i.e., $\left|\omega_n^{(r)}\right|$, which accounts for the dampening or growing of the identified structure, and the frequency of the associated harmonic $f^{(r)}$ (Eq. (8)).

$$f^{(r)} = \frac{\arg\left(\omega_n^{(r)}\right)}{2\pi} f_s \tag{8}$$

Where $arg(\omega_n^{(r)})$ is the argument of the eigenvalue $\omega_n^{(r)}$.

The spectra of λ_n indicating the level of the kinetic energy across the POD modes together with their cumulative energy distribution are plotted in Fig. 5 for the datasets of the test cases TC1 and TC2 ($\omega/2\pi = 29.9$ Hz and 26.3 Hz, respectively). For the case TC1, the first couple of modes #1 and #2 participates for 12.7% and 11.5% to the build-up of the total kinetic energy. Slightly higher efficiency in the decomposition is observed for the case TC2, by which modes #1 and #2 capture 14.2% and 12.2% of the total kinetic energy. This effect can be ascribed to the finer discretization of each cycle having in the dataset of TC2, indeed the spacing between two consecutive azimuthal angles is $\Delta\Psi = 4.4°$.

Scatter plot of the normalized time coefficients of the first pair of POD modes $\mu_1(t)/\sqrt{\lambda_1}$ and $\mu_2(t)/\sqrt{\lambda_2}$ for the test case TC1 is presented in Fig. 6 (a) together with a circumference of radius 1 in red as reference. The correlation of the time coefficients scatters around the theoretical circumference at two different radii. Even though this confirms the periodic behavior of the vortical structures captured by the first pair of POD modes, multiple frequency contents are included into the corresponding time coefficients. Indeed, the plots (b) and (c) of Fig. 6 show the normalized Power Spectral Density (PSD) of $\mu_1(t)$ and $\mu_2(t)$.

Their spectral content exhibits multiple peaks of frequency, here presented in nondimensional coordinate by the Strouhal number $St = fc/V_h$. A maximum is reached at $St = 1.086$, i.e., $f = 119.7$ Hz (~4 × 29.9 Hz) the tip vortex shedding frequency. Secondary peaks are observed across the spectrum and staggered of $\Delta St = 0.27$ ($\Delta f = 29.9$ Hz) from the main detected frequency. Hence, events of coherent structures pulse at slower frequency containing kinetic energy of intensity of the order of the tip vortex shedding.
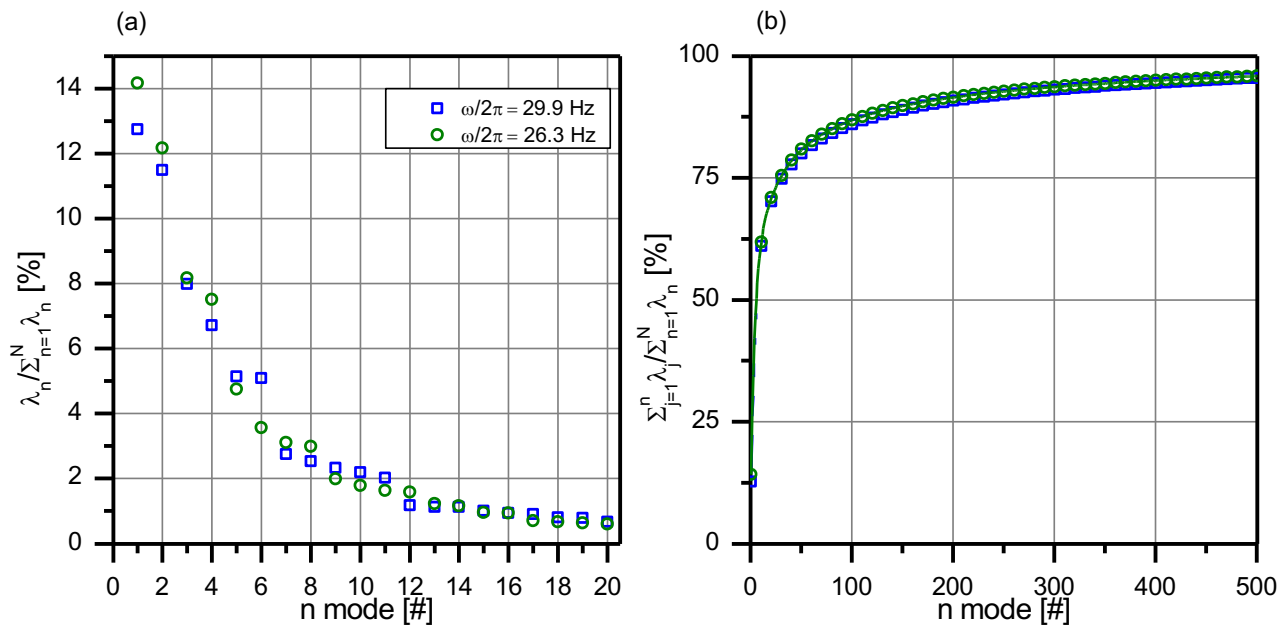
Fig. 5 Spectra of the eigenvalues λ_n in percentage across the first 20 modes (a) and the cumulative energy distributions (symbols placed every 10 points) within the first 500 modes (b) for the test cases TC1 and TC2 ($\omega/2\pi$ = 29.9 Hz and 26.3 Hz, respectively).
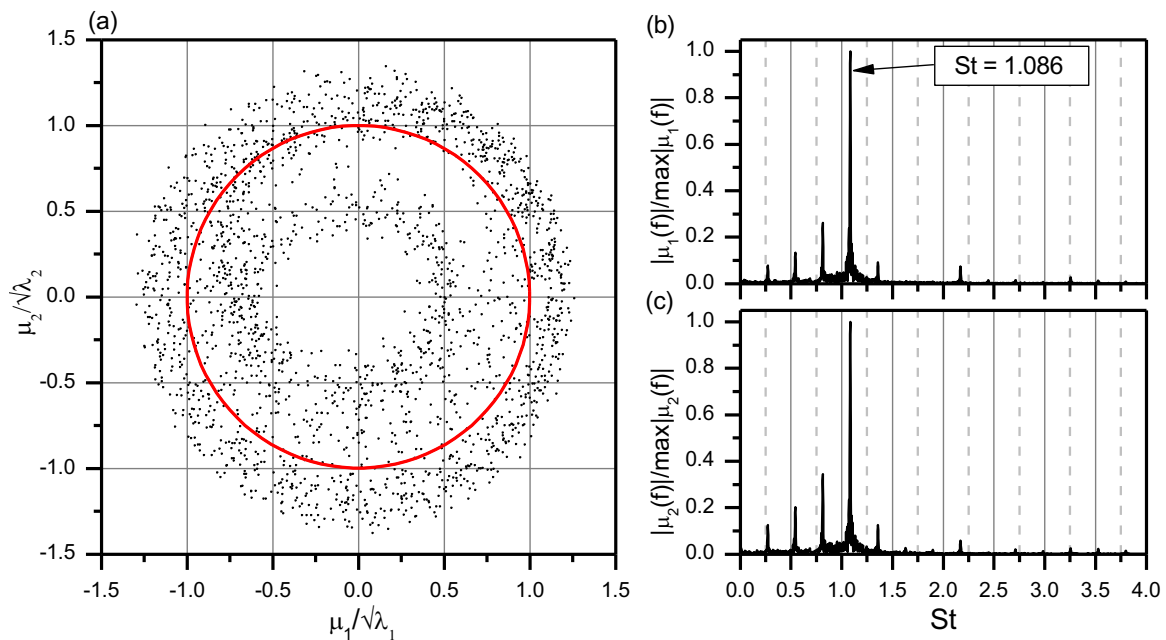

Fig. 6 Scatter plot of the normalized time coefficients $\mu_1(t)/\sqrt{\lambda_1}$ and $\mu_2(t)/\sqrt{\lambda_2}$ with the red circumference of radius 1 (a), spectra of their normalized power spectral densities $|\mu_1(f)|/max|\mu_1(f)|$ (b) and $|\mu_2(f)|/max|\mu_2(f)|$ (c) for TC1 ($\omega/2\pi$ = 29.9 Hz).

For the test case TC2 ($\omega/2\pi$ = 26.3 Hz), the correlation of the time coefficients in the neighborhood of the theoretical circumference of radius 1 indicates the prominence of a single frequency captured into the first pair of POD modes as shown in **Fig. 7** (a). Indeed, their normalized spectra

$|\mu_1(f)|/max|\mu_1(f)|$ and $|\mu_2(f)|/max|\mu_2(f)|$ exhibit in each plot a maximum peak at $St = 1.081$ (**Fig. 7** b and c). Additional peaks feature each spectrum across the maximum, similarly as observed for TC1, they are frequency-spaced by a quantity related to the angular velocity of the rotor ($\omega = 2\pi\cdot26.3$ Hz). The POD decomposition of the dataset of TC2 presents a more pronounced spectral purity for the first pair of modes, which can be ascribed by the finer sampling of each cycle.
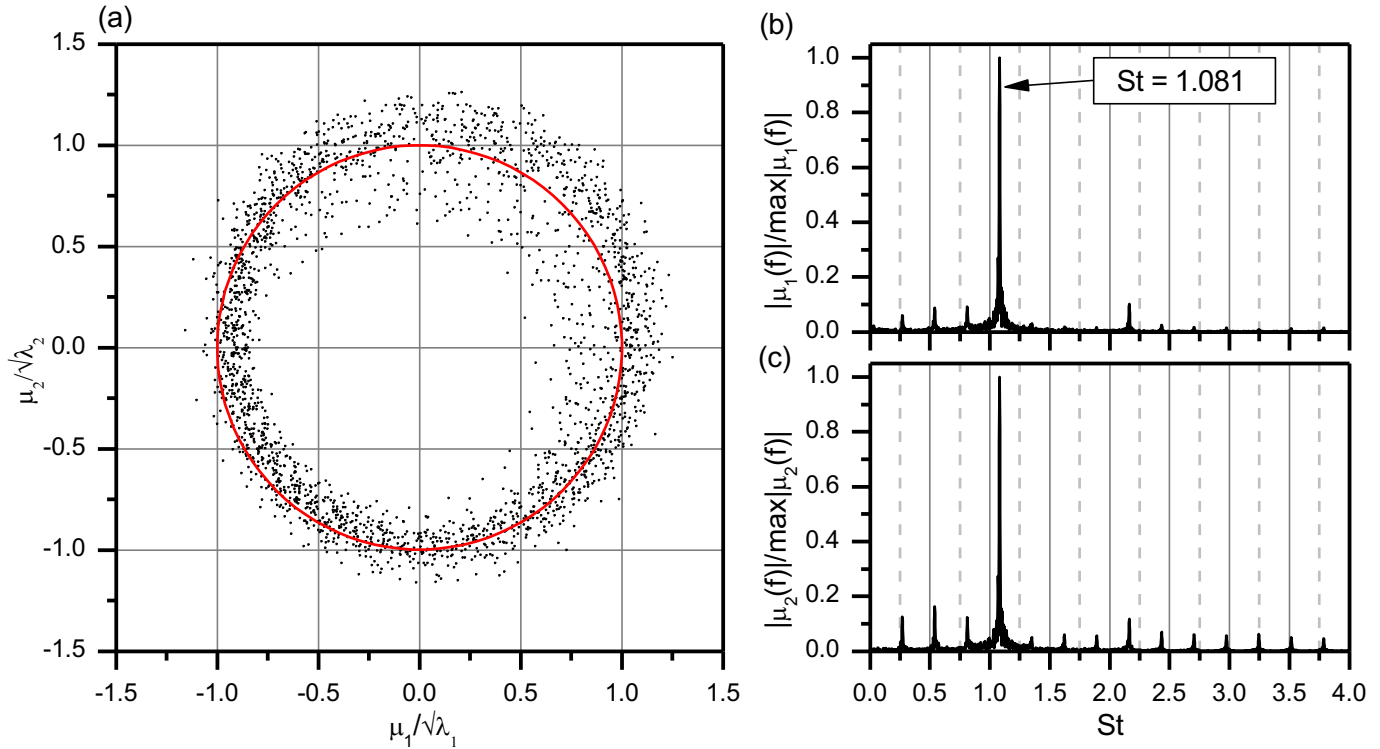

Fig. 7 Scatter plot of the normalized time coefficients $\mu_1(t)/\sqrt{\lambda_1}$ and $\mu_2(t)/\sqrt{\lambda_2}$ with the red circumference of radius 1 (a), spectra of their normalized power spectral densities $|\mu_1(f)|/max|\mu_1(f)|$ (b) and $|\mu_2(f)|/max|\mu_2(f)|$ (c) for TC2 ($\omega/2\pi = 26.3$ Hz).

Fig. 5 shows that the first eleven POD modes capture about ~60% of the kinetic energy, there are pairs (#1-2, #3-4, #5-6, #8-9 and #10-11) shifted by $\pi/2$ describing travelling vortical structures and waves. For conciseness, maps of the POD modes of only one mode for each pair is considered. In Fig. 8, the spatial organization of mode #1 is illustrated by the iso-contours of $|\underline{\varphi_1}(\underline{X})|$ with iso-lines of $Qc^2/V_h^2 = 1$ in red for TC1 (a) and TC2 (b), where Q is the second invariant of the velocity gradient tensor, namely Q-criterion (Jeong & Fazle, 1995). The imprint of the tip vortices along the vertical direction is clearly identified, their coherence persists from $Z/R = 0$ down to -0.16. For TC1 (Fig. 8 a), the iso-lines of Q reveal the coexistence of two vortices interacting, close to each other around $-0.26 \leq Z/R \leq -0.20$, indicating the paring process already discussed for the instantaneous

velocity fields. This effect weakens for the test case at lower angular speed $\omega/2\pi = 26.3$ Hz (TC2) as testified by their spatial organization shown in Fig. 8 (b).
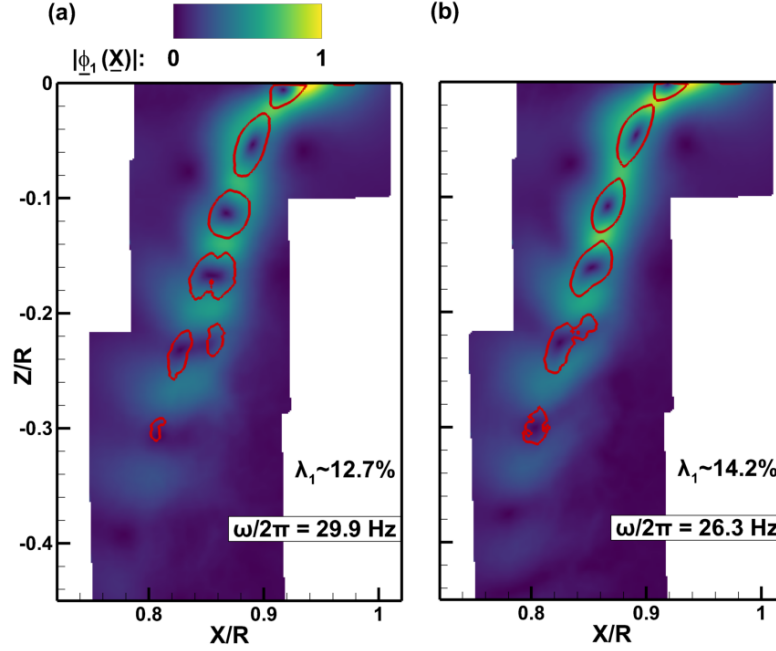

Fig. 8 Iso-contours of module of the POD mode #1, $\left|\varphi_1(X)\right|$, for TC1 (a) and TC2 (b). Vortex imprint visualized using Q-criterion by isolines of $Qc^2/V_h^2 = 1$ in red.

The DMD analysis was conducted by reducing the linear operator A, in Eq.(6), considering a $r = N - 1$ projection onto POD modes, i.e., a space of lower dimension and computationally affordable (Schmid, 2010). The spectra of the eigenvalues $\omega_n^{(r)}$ are inspected in terms of their modulus $\left|\omega_n^{(r)}\right|$ as a function of the Strouhal number, $St^{(r)} = f^{(r)}c/V_h$, associated with the harmonic frequency $f^{(r)}$ already formulated in Eq. (8). In Fig. 9, only the positive semi-axis of $St^{(r)}$ is considered and the first two dominant modes, i.e., $\left|\omega_n^{(r)}\right| \approx 1$, are selected. For TC1 (**Fig. 9** a), the first dominant peak attains to ~0.9986 at $St^{(r)} = 1.09$ ($f^{(r)} = 120.1$ Hz), which is close in value to the shedding frequency of the tip vortices (4×29.9 Hz). The corresponding DMD mode, $\underline{\varphi}_{78}^{(r)}(X)$, in its real and imaginary parts, presents the spatial organization of the coherent structures similar to that observed for the first pair of POD modes of TC1. Hence, for the sake of conciseness they are not shown herein. The DMD modes present similar features to the POD ones because, for this application, the POD provides a harmonic decomposition, so that the modal amplitudes and time coefficients are approximately sinusoidal in time at harmonic dominant frequencies of the tip vortex shedding. Whereas, the second peak of ~0.9965, found at $St^{(r)} = 0.27$ ($f^{(r)} = 29.9$ Hz), identifies the pulsation of the rotor wake having a frequency of $\omega/2\pi = 29.9$ Hz. The corresponding DMD mode, $\underline{\varphi}_{125}^{(r)}(X)$, presents its real part featured by peak activity in region where is located the shear layer as illustrated in **Fig. 10** (a). The imaginary part describes the organization of large-scale coherent

structures localized in the bottom of the inspected region (**Fig. 10** b). This confirms the slower dynamic of the captured flow features.
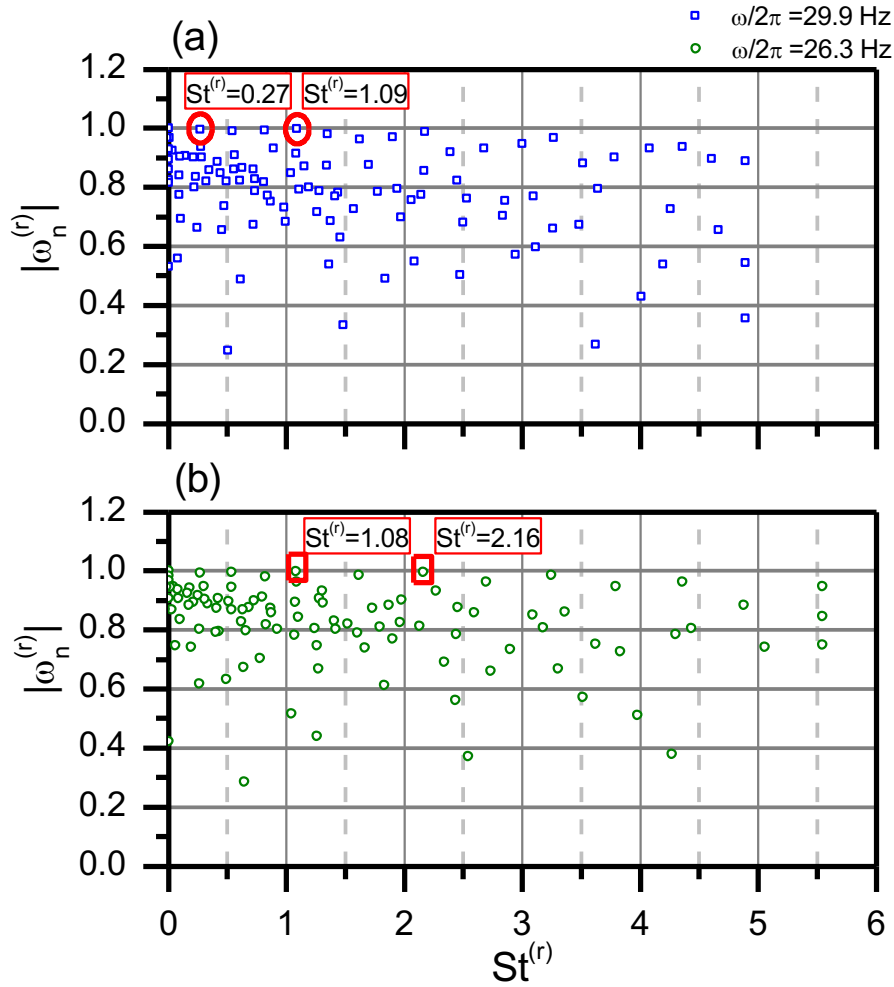

Fig. 9 Spectra of the DMD eigenvalues $\omega_n^{(r)}$ as a function of the Strouhal number $St^{(r)}$ for the test cases TC1 at $\omega/2\pi = 29.9$ Hz (a) and TC2 $\omega/2\pi = 26.3$ Hz (b). Red markers indicate the most relevant dominant modes ($\left|\omega_n^{(r)}\right| \approx 1$).

Similar observation can be retrieved by the inspection of the first dominant peak ($\left|\omega_{80}^{(r)}\right| = 0.9988$) found at $St^{(r)} = 1.08$ ($f^{(r)} = 105.3$ Hz) of the spectra of $\omega_n^{(r)}$ for TC2 shown in **Fig. 9** (b). They are associated with the dynamic of the shedding of the tip vortices as testified by the spatial organization of the flow features captured in the corresponding eigenmode $\underline{\varphi}_{80}^{(r)}(\underline{X})$ (again not shown for brevity). On the other hand, the second peak identifies a higher harmonic at $St^{(r)} = 2.16$ ($f^{(r)} = 210.7$ Hz), i.e., approximately double times by the shedding frequency of the tip vortices for TC2 (4×26.3 Hz). The corresponding DMD mode, $\underline{\varphi}_{30}^{(r)}(\underline{X})$, is shown in **Fig. 11** by the maps of the real part with isolines of $Qc^2/V_h^2 = 1$. Small vortical structures are identified in the shear layer region pulsating at a doubled frequency with respect to that due to the evolution of the tip vortices.

This high frequency harmonic can acoustically interact with the blade by triggering persistent stress, which can induce to severe wear on the blade structures.
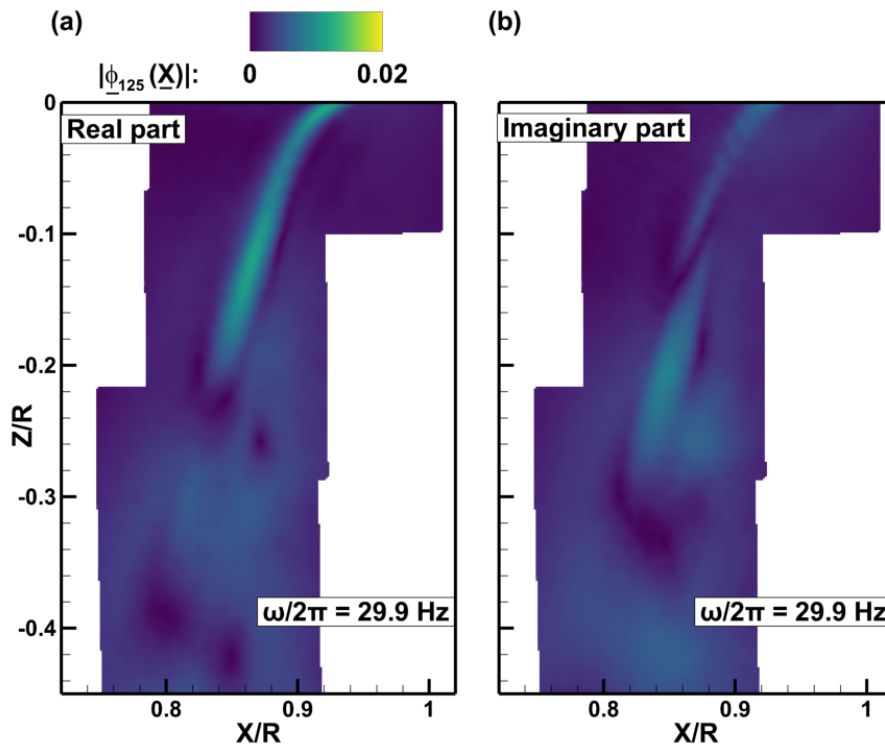

Fig. 10 Iso-contours of module of the DMD mode #125, $\left|\underline{\varphi}_{125}(\underline{X})\right|$, decomposed in its real (a) and imaginary (b) parts for TC1.
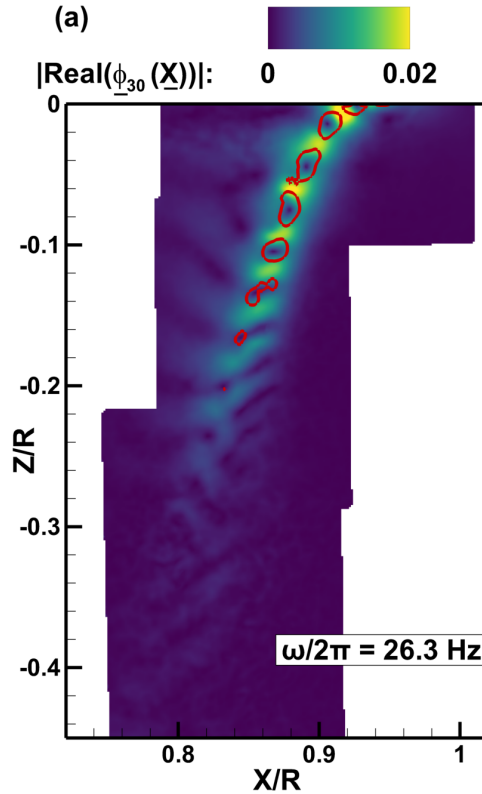
Fig. 11 Iso-contour of module of the real part of the DMD mode #30, $\left|Real(\underline{\varphi}_{30}(\underline{X}))\right|$, for TC2. Vortex imprint visualized using Q-criterion by isolines of $Qc^2/V_h^2 = 1$ in red.

4   Conclusions

An experimental investigation on the tip vortices of a four-bladed isolated rotor has been carried out in hover flight at two rotational speeds either ω = 2π·29.9 Hz (TC1) or 2π·26.3 Hz (TC2) by means of TR-PIV measurements. In turn, the rotor disk generates aerodynamic loads for a thrust coefficient C_T = 5.5 × 10⁻³ or 5.4 × 10⁻³ along the vertical direction in either TC1 or TC2, respectively. The corresponding torque applied to the rotor axis leads to reaching a figure of merit either of *FM* = 0.47 or 0.46. Data-driven analyses, i.e., POD and DMD methods, were considered as decomposition approaches to unveil the basic spatial organization and dynamic of the flow structures.

The inspection of the time-average flow fields shows the wake contraction right at the bottom of the rotor disk inward along the radial direction. This is more pronounced as the thrust coefficient diminishes. The statistical analysis of the velocity fluctuations reveals the imprint of the vortical paths forming multiple inclinations with respect to the vertical direction.

The evolution of the tip vortices from the shedding down to the rotor wake has been conducted by exploring the instantaneous flow fields during one blade revolution. The aged tip vortices are advected downstream by adding momentum from the ambient quiescent air. Under instabilities

by the interaction of oncoming vortices, the pairing process takes place at a certain distance from the rotor disk with the merging of two consecutive co-rotating vortices.

Both modal decompositions present the prominence of the periodic shedding of the tip vortices. The most energetic POD modes, i.e., the first pair, capture the spatial organization of the tip vortices and the pairing event. It is found that they are associated with multiple frequency contents with the dominance of the frequency of the tip vortices St = 1.086 and 1.081 for TC1 and TC2, respectively. Similarly, the dominant DMD modes reflect the periodicity imposed by the tip vortex evolution. For TC1, the rotor wake has a pulsation at the rotor frequency, their modes are characterized by coherent structures having larger diameters than the tip vortices. On the other hand, for TC2, the dominance of small vortical structures is observed pulsating at a doubled frequency than that of the tip vortices.

References

Bhagwat, M. J., & Leishman, G. J. (2000). Correlation of helicopter rotor tip vortex measurements. *AIAA Journal, 38(2)*, 301-308.

Braukmann, J. N., Wolf, C. C., Goerttler, A., & Markus, R. (2019). Blade Tip Vortex System of a Rotor with Cyclic Pitch. *AIAA JOURNAL, 58(7)*, 2869-2880. doi:https://doi.org/10.2514/1.J058678

Brocklehurst, A., & Barakos, G. N. (2013). A review of helicopter rotor blade tip shapes. *Progress in Aerospace Sciences*, 56, 35–74.

De Gregorio, F., Pengel, K., & Kolja, K. (2012). A comprehensive PIV measurement campaign on a fully equipped helicopter model. *Experiments in fluids, 53(1)*, 37-49.

De Gregorio, F., Visingardi, A., & Iuso, G. (2021). An Experimental-Numerical Investigation of the Wake Structure of a Hovering Rotor by PIV Combined with a Vortex Detection Criterion. *Energies, 14(9)*, 2613.

Jain, R., & Conlisk, A. (2000). Interaction of Tip-Vortices in the Wake of a Two-Bladed Rotor in Axial Flight. *Journal of the American Helicopter Society, 45(3)*, 157-164.

Jeong, J., & Fazle, H. (1995). On the identification of a vortex. *Journal of fluid mechanics, 285*, 69-94.

Leishman, J., & Bagai, A. (1998). Challenges in understanding the vortex dynamics of helicopter rotor wakes. *AIAA Journal, 36(7)*, 1130-1140.

Mula, S. M., & Tinney, C. E. (2015). A study of the turbulence within a spiralling vortex filament using proper orthogonal decomposition. *Journal of Fluid Mechanics, 769*, 570-589.

Prouty, R. (1985). Ground effect and the helicopter-a summary. *AIAA Paper 85-4034, in Aircraft Design Systems and Operations Meeting,* (pp. 14-16). Colorado Springs.

Raffel, M., Mulleners, K., Kindler, K., & Heineck, J. (2012). Particle Image Velocimetry in helicopter aerodynamics: developments, challenges, and trends. *American Helicopter Society 68th Annual Forum, 9.*

Raffel, M., Willert, C., Wereley, S., & Kompenhans, J. (2007). Particle Image Velocimetry - A Practical Guide. 2nd Edition, Springer.

Ramasamy, M., & Leishman, G. J. (2004). Interdependence of Diffusion and Straining of Helicopter Blade Tip Vortices. *Journal of Aircraft, 41(5),* 1014-1024.

Ramasamy, M., Johnson, B., & Leishman, G. J. (2009). Turbulent Tip Vortex Measurements Using Dual-Plane Stereoscopic Particle Image Velocimetry. *AIAA Journal, 47(8),* 1826-1840.

Richard, H., Bosbach, J., Henning, A., Raffel, M., Willert, C., & van der Wall, B. G. (2006). 2C and 3C PIV Measurements on a Rotor in Hover Condition. *13th International Symposium on Applications of Laser Techniques to Fluid Mechanics.* Lisbon.

Rossow, V. J. (1985). *Effect of Ground and/or Ceiling Planes on Thrust of Rotors in Hover.* NASA Technical Memorandum 86754.

Schmid, P. J. (2010, August 10). Dynamic mode decomposition of numerical and experimental data. *Journal of Fluid Mechanics, 656,* 5-28. doi:https://doi.org/10.1017/S0022112010001217

Sirovich, L. (1987). Turbulence and the dynamics of coherent structures. I. Coherent structures. *Quarterly of applied mathematics, 45(3),* 561-571.

Westerweel, J., & Scarano, F. (2005). Universal outlier detection for PIV data. *Experiments in Fluids, 39(5),* 1096-1100.

Wieneke, B. (2015). PIV uncertainty quantification from correlation statistics. *Measurement Science and Technology, 26(7),* 074002-10.

Wieneke, B. (2017). PIV Uncertainty Quantification and Beyond. Delft, The Netherlands: ISBN: 978-94-92516-88-6.